Accepted Manuscript

Superstructures of doped yttrium aluminates for luminescent and advanced forensic investigations

G.P. Darshan, H.B. Premkumar, H. Nagabhushana, S.C. Sharma, B. Daruka Prasad, S.C. Prashantha, R.B. Basavaraj

PII: S0925-8388(16)31605-X

DOI: 10.1016/j.jallcom.2016.05.255

Reference: JALCOM 37775

To appear in: *Journal of Alloys and Compounds*

Received Date: 21 January 2016

Revised Date: 18 May 2016

Accepted Date: 22 May 2016

Please cite this article as: G.P. Darshan, H.B. Premkumar, H. Nagabhushana, S.C. Sharma, B. Daruka Prasad, S.C. Prashantha, R.B. Basavaraj, Superstructures of doped yttrium aluminates for luminescent and advanced forensic investigations, *Journal of Alloys and Compounds* (2016), doi: 10.1016/j.jallcom.2016.05.255.

Superstructures of doped yttrium aluminates for luminescent and advanced forensic investigations

G.P Darshan[1, 2], H. B Premkumar,[3,*], H. Nagabhushana[4,*], S. C Sharma[5], B. Daruka Prasad[6],S. C. Prashantha[7], R. B. Basavaraj[4]

[1]Department of Physics, Acharya Institute of Graduate Studies, Bangalore 560 107, India
[2]Research and Development Center, Bharathiar University, Coimbatore 641046, India
[3]Department of Physics, Dayananda Sagar Academy of Technology and Management, Bangalore 560082, India
[4]Center for Nano Research (CNR), Tumkur University, Tumkur 572 103, India
[5]Dayananda Sagar University, Shavige Malleshwara Hills, Bangalore- 560078, India
[6]Department of Physics, BMS Institute of Technology, VTU-affiliated, Bangalore 560 064, India
[7]Department of Science, East West Institute of Technology, Bangalore 560 091, India

Abstract

Nanocrystalline Tb^{3+} (1–11mol %) doped $YAlO_3$ phosphors were prepared by biocompatible combustion route using *Aloe Vera* gel as a fuel. The average crystallite sizes were estimated using XRD and TEM found to be ~27 nm. Scanning electron micrographs showed mcirolayered superstructurs of various shapes of uniform particles. Upon 341 nm excitation, the photoemission profile of $YAlO_3$: Tb^{3+} exhibit a narrow green emission peak at 545 nm due to $^5D_4 \rightarrow {}^7F_5$ transition. Optical parameters such as Judd–Ofelt parameters, radiative transition probabilities, radiative lifetimes, branching ratio, stimulated emission cross-section and optical gain were estimated by Judd–Ofelt theory. CIE coordinate for the optimized phosphor was (x=0.308, y=0.435) which is very close to NTSC standard value for green emission. Further, the correlated color temperature was estimated and found to be ~ 6178 K. A simple, fast, highly sensitive and ecofriendly method for the detection and enhancement of fingermarks in various forensic relevant materials was presented.

KEYWORDS: Bio mediated synthesis; Morphology; Photoluminescence; Judd-Ofelt analysis; latent fingerprint.

* Corresponding authors. Tel.: +91-9880433880, E-mail: premhb@gmail.com (H B Premkumar), +91- 9945954010,E-mail addresses:bhushanvlc@gmail.com (H.Nagabhushana)

1. Introduction

In recent years there is a requirement of light emitting devices which are of low cost, capable of producing in large amount and efficient light emission ability. In this regard, few different concepts have been used to attain light emitters such as: quantum wells [1], quantum dots [2], nanocrystals [3–5], nanowires [6] and thin films [7]. The light emitting devices of various spectral range have been used in X- and γ -ray detectors [8, 9], large size displays, lasers, amplifiers [10, 11], eco-friendly and efficient lamps, scintillators [8, 12, 13] etc. This has been achieved by selecting a proper host material and optimized dopants preferably the aluminates and rare earth ions respectively.

Among the various hosts, yttrium aluminate ($YAlO_3$) has two familiar crystal phases: orthorhombic and hexagonal [14]. Till date cubic and hexagonal phases were well documented in the literature but not on the orthorhombic phase of $YAlO_3$. The rare earth ions (RE^{3+}) characterize with a narrow emission lines in the UV and IR range due to their precise electronic configuration.

The various processing techniques, which are used for the synthesis of $YAlO_3$ nanophosphor, include microwave refluxing, solution combustion, hydrothermal, sol–gel, co-precipitation and precursor thermal decomposition method etc. [15–17]. In these methods, generally the toxic solvents, harsh chemicals, additives and surfactant were used which are not ecofriendly. Hence to overcome from the eco-destructive routes, numerous efforts have been devoted towards green synthesis of metal-oxide nanoparticles using plant and animal extracts contains protein chains, polysaccharides, bacteria, fungi, yeast, viruses etc. [18 - 20]. Phytosynthesis was a beneficial and eco-friendly approach to prepare nanoparticles

using plant extracts from its root, leaf, stem etc. In this paper, extracts of *Aloe Vera (A.V.)* plant with botanical name *Aloe Vera (L) Burm. f.* was used as a fuel to get $YAlO_3:Tb^{3+}$nanophosphor. *A.V.* plant was a juicy plant belongs to the family of Liliaceae. *A.V. gel* contains 75 potentially active constituents: vitamins, enzymes, minerals, sugars, salicyclic acids, lignins, saponins, amino acids, alkaloids and flavones. The biological units such as polysaccharides, protein chains, enzymes etc. in the leaves of *A.V.* helps in various medical applications such as wound healing, antifungal activity, hypoglycemic, anticancer etc. Hence using *A.V.* plant gel as a bio-template helps in obtaining complex superstructures (SS) in the micro / nano level which has been improved the light emitting capacity than the prepared samples in regular route.

Ridge pattern of each creature in the nature has unique and unalterable; hence fingerprint technique in identifying the individual human being is considered as a powerful tool. Latent fingerprints which were generally invisible require a technique to enhance its visualization and identification [21–22]. To improve the quality of fingerprints visibility, forensic investigators generally use optical equipment and/or chemical substances. But these conventional techniques demands for the better adherence of powder particles to fingerprint residues for providing better contrast between the fingerprint profile and the background surface [23]. Predicting the fingerprint by using powders were unable to develop better patterns on the hard surfaces and involves metallic compounds which were hazardous to the users health [24]. These problems can be overcome by using luminescent powders consists of nanoparticles doped with RE. The use of nanoparticles helps in better adhesion efficiency due to its large surface to volume ratio and RE helps in improved

luminescence efficiency. So using RE based luminescence nanopowders can be used as a better labeling agent than the existing once.

In this paper, *A.V.* plant gel mediated combustion method was used for the synthesis of $YAlO_3:Tb^{3+}$. Here *A.V.* plant gel acts as a fuel /sacrificial bio-template and Tb^{3+} ions acts as an efficient green emitter in the host of $YAlO_3$ matrix.

2. Experimental

2.1 Synthesis

The chemicals, yttrium nitrate [Y $(NO_3)_3$. $4H_2O$ (99.9%)], aluminum nitrate [Al $(NO_3)_3$ $9H_2O$ (99.9%)] and terbium nitrate [Tb $(NO_3)_3$ (99.9%] were used as oxidizers and *A.V.* gel extract as a fuel respectively. *A.V.* gel was collected from the fresh leaves of *A.V.* plant which is free from disease. It was collected in the month of July/August 2015 from Tumkur University campus located at 13° 20' N, 77° 08' E. The procedure to collect and its use during the preparation was according to the previous literature reported by Patel et al. [25]. The freshly obtained *A.V.* gel was characterized by their viscosity, optical density and refractive index and found to be 0.545 ± 0.007 cm^2s^{-1}, 1.17 ± 0.04 abs and 1.3323 ± 0.0002 respectively. The metal nitrates and *A.V.* gel were dissolved in double distilled water and then mixed using magnetic stirrer for 25 min to get clear solutions. For the fresh *A.V.* gel content of 10 ml, 15 ml, 20 ml, 25 ml and 30 ml, the obtained concentration of active agents were 0.0376, 0.0713, 0.138, 0.337 and 0.476 $mol.dm^{-3}$ respectively estimated based on the molecular weights and the contents of water which is according to the stoichiometric method. The resultant solutions were kept in a pre-heated muffle furnace maintained at 400 ± 10 ^oC for the combustion process which breaks the polymeric network and helps in obtaining the pure sample. During the combustion,

the flame persists for ~ 1 min and the entire combustion process undergone as a smoldering type. After the completion of the combustion process, the dish was taken out of the furnace and the powder was calcined at 1000 ^{o}C for 3 h to obtain the required phase. The prepared samples were characterized for their nano/micro regime and then optical studies were carried out along with their use to improve the latent finger print studies.

2.2 Characterization

The phase purity and the crystallites of the nanophosphor were examined by powder x-ray diffractometer (Shimadzu) using Cuk$_{\alpha}$ (1.541 Å) radiation. The surface morphology of the prepared samples was studied by scanning electron microscopy, Hitachi table top – (SEM Model - TM 3000). Hitachi H-8100 (voltage-200 KV, LaB_6 filament) equipped with EDS (Kevex sigma TM Quasar, USA) was used for transmission electron microscopy. The FT-IR studies were performed on a Perkin Elmer Spectrometer (Spectrum 1000) with KBr pellets. SL 159 ELICO UV- Vis spectrometer was used to study the UV-Vis absorption studies. Jobin Yvon Spectroflourimeter Fluorolog-3 equipped with 450W Xenon lamp as an excitation source was used for the photoluminescence (PL) studies.

2.3 Footing for fingerprint technique

Fresh fingerprints from healthy donors were deposited on different non-porous **(**glass, aluminum foil, polythene bag**),** semi-porous (knife handle) and porous (freshly cut green leaf) surfaces with medium pressure. The fingers of the donor were cleaned with soap water and exposed to dry air for 10 min to confirm reliability of the study. The prepared fluorescent nano powders were brushed sensibly to make sure about the

uniform spread on the latent fingerprint surfaces. Then the surfaces were illuminated with UV lamp (4 W, 254 nm) and the images of the fingerprint were photographed using a digital camera in situ with a Nikon D3100 digital camera equipped with AF-S Nikkor 50 mm f/l.8 G ED lens.

3. Results and Discussion

Fig.1 shows the powder X-ray diffraction (PXRD) patterns of the $YAlO_3:Tb^{3+}$ (1-11 mol %) nanophosphor. The diffraction peaks were well matched with standard JCPDS File no. 70-1677 of orthorhombic phase of $YAlO_3$ with negligible traces of $Y_3Al_5O_{12}$ phase [26]. Peak broadening was estimated for all the major peaks to determine the average crystallite size (D) using Scherer's formula:

$$D = \frac{0.9\lambda}{\beta \cos\theta} \qquad \text{---------- (1)}$$

where λ ; the incident wavelength of Cukα - X-ray, θ ; the Bragg's angle and β; the FWHM in radian. The value of D was found to be in the range 20-30 nm tabulated in Table.1.

The structural information of $YAlO_3$: Tb^{3+} (7 mol %) sample was analyzed precisely by the Rietveld refinement using *FULLPROF* suit program [27]. In this case Pseudo-Voigt function [28] was used to fit the several parameters to the data point. The refined parameters namely occupancy parameter, atomic positional values were summarized in Table.2. Better statistical validity was observed between the experimental relative intensity (observed XRD intensities) and statistically estimated intensity (Fig. 2). Further, the quality of the refined data was checked by estimating goodness of Fit (GoF) = $\chi^2 = (R_p/R_{wp})^2$ = 1.06 which suggests that the studied phosphor was in highly crystallinity and good refinement. By utilizing the Rietveld

refinement parameters, the packing diagram was drawn using Diamond software (Inset of Fig. 2.).

According to the crystal field theory, the acceptable percentage difference the ionic radii of doped and host ions must be less than 30 % as estimated using the relation.

$$D_r = \frac{R_m - R_d}{R_m} \quad \text{---------- (2)}$$

where R_m and R_d ; radii of host material and dopant ion. The Tb^{3+} ionic radius and coordination number were close to that of Y^{3+}, hence Tb^{3+} ions easily replaces Y^{3+} in the $YAlO_3$ host because of D_r which is equal to 1.39 % [29].

Fig. 3(a) shows the SEM micrograph of the $YAlO_3$:Tb^{3+} (7 mol %) prepared using 10 ml of *A.V.* gel; shows the occurrence of tidy SS consists of layered beds organized one above the other resembles the group of layered nests. With increase in *A.V.* gel content, the morphology changes from layered assemblies to pointed layered assemblies to boat shape assemblies to closed assemblies of microstructures. Hence *A.V.* content was utilized in wrapping of nanoparticles layers to form micro/nano superstructures (SS). Fig. 3 (b) shows the pointed layered structures oriented to various planes resembles the outer layer of jackfruit. Fig. 3(c) & 3(d) shows the columnar SS with top layer resembles the boat shape for both 20 ml and 25 ml concentrations of *A.V.* gel. But the size of the boat-SS found to increase with *A.V.* content from 20 to 25 ml. After 25 ml concentration, the opened structures again wrapped into the closed structures form the bullet like shapes (Fig. 3(e)). This type of shapes were common in dry soil structures formed due to the electrostatic forces that attracted the particles to group together and forms the SS of the micro/nanoparticles.

To show the similar kind of naturally occurring textures, the photograph of dry soil texture was shown in Fig. 3 (f). SEM study confirms the role of *A.V.* content strive as a sacrificial unit in the formation of SS.

For different *A.V.* concentration, the different morphologies obtained were because of the formation of the temporary polymeric network at the time of mixing which decomposes to an ordered form, when subjected to heat treatment. At the time of heat treatment, the effective heat was distributed in complex manner to break the formed polymeric networks. The rate of crystal growth was faster at low temperature and changes gradually with elevated temperatures. The Y^{3+} and Tb^{3+} ions gets blended with polysaccharide of different kind and protein chains through electrostatic interaction with O(-ve) ions. During stirring process, free amino and carboxylic groups interact with the micro/nano-SS results the temporary polymer networks. The functional groups and proteins present in the medium act as capping ligands and preventive units to minimize the agglomeration.

The sugar molecules of *A.V.* such as galactose, pectin and acetylmanose etc are linked into the chains of variable lengths. The polysaccharide like pectin was considered and shown the network of this organic chain along with proteins trap the $YAlO_3:Tb^{3+}$ nano-dimension particles and the network acts as a sacrificing element. So during the process of combustion, the network disappears leaving behind the specific shape and structures of the nanopowder material. The mechanism of the network was shown in Fig. 4. An appropriate model to explain these mechanisms is called the “egg box model”. In which the polysaccharide molecules interact with cations to form bridges of two carboxyl groups of galactose / acetylmanose / pectin groups of the two different chains which were close to each other. The cations

maintain the molecules together and form SS with supportive binding of two or more chains of adjacent polysaccharide. The polymeric binding was responsible for the aggregation of contents of the gel and shows a coherence effect to obtain the complex structures. Further, by changing the interaction of proteins and polysaccharides as attractive or repulsive interaction the SS formation can be tuned as surface with opened structures or with closed structures as shown in SEM images of Fig. 3.

To support for the SEM analysis, the $YAlO_3:Tb^{3+}$ (7 mol %) powder was characterized by TEM and was shown in Figs. 5 (a and b). The TEM images clearly shows the pointed edges of about 44 nm and the links between the different layers were also observed in Fig. 5 b. The pointed edges and the SS links were marked in TEM images of two different resolutions. The crystallite size of the nanomaterials was in good agreement with the PXRD. Fig. 5(c) shows the EDAX; confirms the elements present in the sample and thereby it confirms the purity of the sample; however the identified carbon and copper were due to grid used for TEM studies.

Inset of Fig. 6 shows the diffused reflectance spectra of $YAlO_3:Tb^{3+}$ phosphor material recorded in the wavelength region of 200–600 nm using UV-Vis spectrometer. The maximum absorption at 252 nm may be due to the transitions between the upper levels of valence band to the lower level of conduction band which is nothing but the optical energy gap (E_g) [30, 31]. The E_g values were estimated using Tauc relation [32]. The estimated direct E_g values were found to be in the range 5.45–5.59 eV (Fig.8) which is in good agreement with the literature [33]. This signify that the allowed direct E_g was responsible for the inter band transitions and it is generally depends on the synthesis method and experimental conditions which can favor or inhibit the formation of structural defects.

The functional group analysis was done by FTIR technique was shown in Fig. 7. The band at 3442 cm^{-1} can be allocated to vibration mode of chemically bonded water molecule. The band at 1510 cm^{-1} was attributed to the bending mode of H–O–H vibrations. Three sharp peaks at 455, 561 and 690 cm^{-1} were due to the stretching mode of the AlO_6 octahedral units [34] and were in agreement with PXRD patterns.

Inset of Fig. 8 shows the excitation spectrum of Tb^{3+} (7 mol %) doped $YAlO_3$ monitored at 543 nm. A wide excitation band in the range 300–400 nm observed was due to the intra-configurationally (f–f) transitions of Tb^{3+}. It can be related to O^{2-} - Tb^{3+} charge transfer band (CTB) based on the empirical formula [35]

$$E_{ct}\left(cm^{-1}\right)=\left[\chi_{opt}(X)-\chi_{opt}(M)\right]\times 30{,}000\,cm^{-1} \qquad \text{------ (3)}$$

χ_{opt}(X) and χ_{opt} (M) ; the opto-electro negativities of the oxygen and metal cation respectively. The opto-electro negativity of O^{2-} was variable in different hosts, thus by putting χ_{opt} (O^{2-}) = 3.2 and χ_{opt} (Tb^{3+}) = 0.95 [36] into Eq. (3), the position of O^{2-} $\rightarrow Tb^{3+}$ CTB can be calculated to be 160 nm. For Tb^{3+} ions, when one electron was promoted from ground state ($4f^8$) to excited state ($4f^75d^1$), it gives the transitions such as spin-allowed (SA) ($^7F_J \rightarrow {}^7D_J$) and spin-forbidden (SF) ($^7F_J \rightarrow {}^9D_J$) corresponds to stronger intensity with higher energies and the weaker intensity with lower energies respectively. The calculated energies corresponds to SA and SF transitions can be evaluated according to Eq. (4) [37]

$$E\left(Tb,YAlO_3\right)=49{,}340\ cm^{-1}-D(A)+\Delta E^{Tb} \qquad \text{------- (4)}$$

where $E\left(Tb,YAlO_3\right)$; the f–d energy difference of the Tb^{3+} doped ions in the $YAlO_3$ host with the so-called crystal field depression D(A). The energy of the allowed f–d

transitions of Tb^{3+} embedded in the $YAlO_3$ matrix was considered as 13,200 ± 920 cm^{-1} (SA) and 6300 ± 900 cm^{-1} (SF) and with this the estimated E values of ($YAlO_3$), (Tb^{3+}, $YAlO_3$) were 46,003 ± 920 cm^{-1} and 39,103 ± 900 cm^{-1} respectively. The longer wavelength transitions related to $^7F_6$ ground state to the excited levels of the $^4F_8$ configuration. The maximum peaks at 369 and 379 nm were attributed to the transitions $^7F_6 \rightarrow (^5G_6, {}^5G_5, {}^5G_9)$ and $^7F_6 \rightarrow (^5D_3, {}^5L_{10})$ based on the energy level schemes of Tb^{3+} ions [38, 39].

The emission spectra shown in Fig.8 consists of a group of typical $^5D_{3,4} \rightarrow {}^7F_J$ (J = 3, 4, 5 and 6) transitions of Tb^{3+} upon 341 nm excitation, among which the $^5D_4 \rightarrow {}^7F_5$ transition at 545 nm was major corresponds to the bright green light emission. The green emission for wavelength above 490 nm corresponds to the transition $^5D_4 \rightarrow {}^7F_j$ and the blue emission for wavelength below 490 nm corresponds to the transition $^5D_3 \rightarrow {}^7F_j$. Due to the significance of the cross relaxation from the $^5D_3 \rightarrow {}^5D_4$, the intensity of the blue emission peak at 463 nm was much weaker than that of the green emission peaks at 493, 545 and 591 nm [40]. The cross relaxation can be further enhanced by increasing the ion concentration leading to a strong emission of $^5D_4 \rightarrow {}^7F_j$ transition [41, 42]. The corresponding transitions for all the emission bands were listed in Table 3.

The emission intensity of Tb^{3+} as a function of its doping concentration in the host is as shown in Fig.9. PL intensity increased with increase in Tb^{3+} concentration up to 7 mol % and afterwards quenching starts. Initially, the PL intensity increases and then decreases due to comparably but slightly bigger radius of Tb^{3+} (106.3 pm) as compared to Y^{3+} (104 pm) ions. At higher intensity the charge imbalance leads to cross relaxation and on radiative transitions causes concentration quenching [43].

With increase in the concentration of Tb^{3+} ions, the distance between the activator ions decreases which leads to the non-radioactive energy transfer among Tb^{3+} ions [44]. In this context, the critical distance (R_c) can be estimated from the following equation [45]:

$$R_c \approx 2\left(\frac{3V}{4\Pi X_c N}\right)^{\frac{1}{3}} \quad \text{--------- (5)}$$

where V; the volume of the unit cell, X_c; the critical concentration of Tb^{3+} ions and N; the number of sites in the unit cell. Presently, V; 204.10 $Å^3$, X_c; about 0.07 and N;4, resulting in the critical distance of about 11.16 Å. Generally, the resonant energy-transfer is directed by multipolar and exchange interactions. In this study, the energy transfer among Tb^{3+} (1-11 mol %) ions with $YAlO_3$ phosphor does not occur but there is a charge transfer mechanism. Hence the process of energy transfer should be electric multipole interaction. Another important parameter was the asymmetric ratio (A_{21}) [46, 47] which gives a measure of the degree of distortion from inversion symmetry of the local environment surrounding the Tb^{3+} ions in the host matrix.

$$A_{21} = \frac{\oint I_2\left({}^5D_4 \rightarrow {}^7F_5\right)d\lambda}{\oint I_1\left({}^5D_4 \rightarrow {}^7F_6\right)d\lambda} \quad \text{---------- (6)}$$

where I_1 and I_2; intensity of magnetic dipole transition at 493 nm and electric dipole transition at 545 nm respectively. The values of intensity ratios (A_{21}) for $YAlO_3$:Tb^{3+} increases with the increase in Tb^{3+}concentration (Fig. 9). Van Uitert [48 - 50] stated that the intensity of multi- polar interaction can be resolute based on the change in the emission intensity from the emitting level that has multipolar interaction. The emission intensity (I) per activator ion follows the equation;

$$\frac{I}{\chi} = K\left[1+\beta(\chi)^{\frac{Q}{3}}\right]^{-1} \quad \text{---------- (7)}$$

Where χ ; the activator concentration, Q ; a constant of multi- polar interaction and equals 6, 8, or 10 and less than 6 for dipole-dipole; dipole-quadrupole or quadrupole-quadrupole interactions and charge transfer mechanism respectively, and K and β are constants under the same excitation condition for the given host crystal.

$$Log\ \frac{I}{\chi} = A - \frac{Q}{3}\log\chi \quad \text{---------- (8)}$$

where $\left(A = \log k - \log\beta\right)$. The curve of log I/$\chi$ v/s. log χ in $YAlO_3$:Tb^{3+} phosphor was shown in Fig. 10. The figure clearly shows that the relation between log I/χ and logχ was approximately linear and the slope was about -0.869. The Q value calculated based on the linear fitting using Eq. (8) was ~ 2.607, which was less than 6. This finding indicates that the charge transfer mechanism was dominant as explained in earlier paragraphs.

To know the consequence of chemical environment on luminescent properties of Tb^{3+}, J-O theory [51, 52] was utilized and estimated the J-O intensity parameters. In the case of Tb^{3+}, it was possible to determine the Ω_λ (λ=2, 4, 6) parameters from the emission spectra. The measured line strengths S_{mes} ($J \rightarrow J'$) and calculated S_{cal} ($J \rightarrow J'$) of the selected energy bands were estimated from Eqs. 9 and 10 respectively [53, 54]:

$$S_{mes}\left(J \rightarrow J'\right) = \frac{C}{\lambda}\frac{9n_{eff}}{\left(n_{eff}{}^2+2\right)^2}\Gamma_{exc} \quad \text{.....(9)}$$

$$S_{cal}\left(J \rightarrow J'\right) = \sum \Omega_t \left|\left\langle \Phi J \middle\| U^{(t)} \middle\| \Phi' J' \right\rangle\right|^2 \quad \text{------ (10)}$$

where J and J'; the initial and final state angular momentum quantum numbers. C; the proportional constant that includes the calibration factor for the optical detecting system and n_{eff}; effective refractive index of the sample obtained from the quantity of nanoparticles which were occupied in the total matrix of the compound (n_{eff} = 1.915), λ; mean wavelength of the excitation band and Γ_{exc}; the integrated excitation intensity for each band from the initial state to the final state. In Eq. 10, the values of reduced matrix elements of the unit tensor $\left|\left\langle \Phi J \right\| U^{(t)} \left\| \Phi' J' \right\rangle\right|$ were adopted as reported in the literature [55], $<\|U^{(t)}\|>$ were the doubly reduced matrix elements of rank t (t = 2,4,6) between states characterized by the quantum numbers (S, L, J) and (S', L', J'). The parameters Ω_2, Ω_4, and Ω_6 were evaluated using the equation as mentioned in Eqs. 11.

$$\Omega_2 = \frac{3h\lambda_{0-2}A_{0-2}\varepsilon_0}{16\pi^3 e^2 \zeta (0.0032)},\ \Omega_4 = \frac{3h\lambda_{0-4}A_{0-4}\varepsilon_0}{16\pi^3 e^2 \zeta (0.0023)} \text{ and } \Omega_6 = \frac{3h\lambda_{0-6}A_{0-6}\varepsilon_0}{16\pi^3 e^2 \zeta (0.0003)} \quad \text{.....(11)}$$

Where λ ; the wavelength corresponds to the 2nd, 4th and 6th major emission peaks of the PL spectra and A; values were evaluated according to Eqs. 6 and 13 which was explained in the consecutive pages. ζ is the parameter obtained from n_{eff}. The bracket quantity in the denominator represents the matrix elements of the transitions as reported in the literature [56 - 58].

The values of the J-O parameters for the prepared samples were tabulated in Table 4. In general, the parameter Ω_2 was related to the covalency and/or structural changes in the vicinity of the Tb^{3+} ion (short-range effect) and Ω_4 was related to the long-range effects. Ω_6 showed very small quantity which was due to the possibility of the stable state. For long-lived metastable excited states this method is not suitable

but evaluated parameters were presented in the Table.4. The error involved in the estimation of J-O intensity parameters were measured according to the literature by standard deviation method was showed the goodness of the J-O parameters fitting [59]. The values of the J–O parameters were useful to calculate the spectroscopic quality factor $X = \Omega_2/\Omega_4$ which helps in calculating the stimulated emission for the laser active medium. The spectroscopic quality factor of Tb^{3+}:$YAlO_3$ was 6.35 and larger than of other host listed in Table.5, hence it is a promising material for efficient laser action [60]. The radiative transition probabilities (A_T), lifetime (τ_{rad}) and transition branch ratios (β) were important dynamic parameters for trivalent rare earth ions. The τ_{rad} for an excited state (J) was calculated by Eq.12.

$$\tau_{rad} = \frac{1}{\sum A(J - J')} \qquad \text{------ (12)}$$

where the sum is taken over all final lower-lying states J'. The A_T for the transitions determined by using Eq. (13) and reported in Table 5.

$$A(J - J') = \frac{64\prod^4 e^2}{3h(2J+1)\lambda^3} \frac{n(n^2+2)^2}{9} S_{calc}(J - J') \qquad \text{------- (13)}$$

According to Eq. (12), the τ_{rad} of the $^5D_4$ level is determined to be ~ 17.1 ms. The experimental τ_{rad} was found to decrease slightly with increase of Tb^{3+} ions content. It was known that a transition having β of ≥ 0.50 can emit laser radiation more effectively. The measured β of 0.99 for the $^5D_4 \rightarrow {}^7F_5$ transition of 7 mol % Tb^{3+} doped $YAlO_3$ suggests its suitability for green color displaying devices and to some laser devices. The effective emission cross-section (σ_E) was estimated according to Eq. 14.

$$\sigma_E = \frac{\lambda^2}{8\pi c n^2} A_{ed}\left(J'' \rightarrow J'\right) \quad \text{--------- (14)}$$

In Tb^{3+}:$YAlO_3$ phosphor, σ_E was calculated and listed in Table 5. Such nature of long τ_r and σ_E section in Tb^{3+}:$YAlO_3$ is favored for generating low threshold and high efficient lasers. Therefore these materials were suitable as a laser material.

The Commission International De I-Eclairage (CIE) 1931 chromaticity co-ordinates for $YAlO_3$: Tb^{3+} (7 mol %) phosphors were calculated for the optimized Tb^{3+} ion concentration in PL spectra. The CIE values estimated using PL spectra were shown in Fig. 11. It was detected that the CIE co-ordinates (x = 0.30889, y = 0.43592) was in green region and nearly same as the National Television System Committee (NTSC) standard values. The correlated color temperature (CCT) was estimated by Planckian locus indicates the existence of numerous operating points outside the Planckian locus. If the coordinates of a light source falls outside the Planckian locus and the CCT in the range of 6178 K using U' = 0.16229 and V' = 0.51532 (Fig.12). Hence the prepared samples may be useful for the fabrication of artificial white light as green component in white LEDs and display devices.

3.1 Fingerprint detection using $YAlO_3$:Tb^{3+} (7 mol %) nano-phosphor

The optimized $YAlO_3$:Tb^{3+} (7 mol %) nanophosphor was tested for being used in latent fingerprint sensor on smooth non porous surfaces/ semi porous/ porous surfaces. Fig.13 shows the fresh finger print images developed by $YAlO_3$: Tb^{3+} nanophosphor from glass, knife handle, freshly cut green leaf, polythene sheet and aluminium foil. Owing to the nano-sized phosphor they exhibit better adhesion for finger mark ridges. It was noticed that the detailed finger print images from different non porous surfaces excited under UV light (254 nm) showed the green color images

from fingerprint were intense and clear. This indicates that the smooth finger print images with detailed ridge pattern can be captured in a better way using the prepared samples.

Further, due to SS of nanoscale can interact with the amino acid such as sebum-rich fingerprint acts as a dusting powder to locate and visualize fingerprints in a better way even if the prints were faint [60]. Since the green light is in the middle of the visible range, so under UV light excitation, the fingerprint deposited on objects can be readily viewed effectively without the influence of background colors. The semi-porous knife handle and porous surface of freshly cut leaf represent one of the difficult, but commonly encountered substrate for recovering latent fingerprints. The obtained nanophosphor appears to be capable to identify the finger prints with reasonable details. A clear distinguish between fingerprint ridges and background also visible.

3.2 Comparison of fingermark images acquired with different illuminations

From the excitation spectrum and emission spectrum, it is observed that most of the nanophosphors fingermark reagents could only be used under a certain illumination. The development of the latent fingermarks with the natural color; the only way utilized was on light color substrates or dark color substrates. These above unique conditions significantly reduced scope of their application. Whether or not one fingermark reagent could be applied under different excitation illuminations was explored in this part. Fig. 14 shows the fresh fingermark deposited on glass plate under different illuminations. High-quality labeling of fingermarks could be obtained under 254 nm UV, 365 nm near UV and white light. As a simple fingermark reagent, $YAlO_3:Tb^{3+}$ (7 mol %) nanophosphor suspension could help to give good fingermark

images under different conditions. The above results indicate that the optimized $YAlO_3$: Tb^{3+} (7 mol %) nanophosphor is useful as fingerprint labeling agents due to intense photoluminescence.

4. Conclusions

For the first time *A.V.* gel assisted green emitting $YAlO_3$:Tb^{3+} (1– 11mol %) nanophosphors were prepared by sacrificial bio-mediated combustion method. Different shaped SS with porous and pointed edges of micro/nanoscale were observed from SEM studies. TEM micrograph confirms the nanosize of the crystallites in the range 25–35 nm. The materials were showed the insulating nature with the Eg value varies from 5.45–5.59 eV. The phosphor exhibits emission spectra with most intense emission of Tb^{3+} assigned for the transition ($^5D_4 \rightarrow {}^7F_5$) at 545 nm. Intensity and the radiative parameters were justified by J-O analysis. Based on the long radiative life time which is the direct evidence for stimulated emission, the materials may find applications in lasing action. The estimated CIE chromaticity co-ordinates (x, y) were very close to NTSC standard value of green colour emission and corresponding CCT was found to be 6178 K for the prepared samples. Hence, the $YAlO_3$:Tb^{3+} (7 mol %) SS material may be a promising material optical display as well as latent fingerprint detection applications.

Acknowledgements

Author HBP thanks VGST, Government of Karnataka, India, (No VGST/P3/SMYSR/GRD-302/2013-14) for its help in carrying out this research work. The authors SCP, HPN and HBP thanks to VGST, Govt. of Karnataka, India, (No: VGST / CISEE /2012-13/282) for sanctioning the research project.

References

[1]. A. Podhorodecki, J. Andrzejewski, R. Kudrawiec, J. Misiewicz, J. Wojcik, B.J.Robinson, T. Roschuk, D.A. Thompson, P. Mascher, Photoreflectance investigations of quantum well intermixing processes in compressively strained InGaAs*P* / InGaAs*P* quantum well laser structures emitting at 1.55μm, J. Appl. Phys., 100 (2006) 0131111–013111-12.

[2]. D. Bimberg, U.W. Pohl, Quantum dots: promises and accomplishments, Mater. Today, 14 (2011) 388–397.

[3]. Y. Yin, A.P. Alivisatos, Colloidal nanocrystal synthesis and the organic–inorganic interface, Nature, 437(2005) 664-670.

[4]. F. Wang, X. Liu, Recent advances in the chemistry of lanthanide-doped up-conversion nanocrystals, Chem. Soc. Rev., 38(2009) 976–989.

[5]. A. Podhorodecki, Designing, Synthesis and Optical Properties of Ultra small β-$NaYF_4$ Nanocrystals Doped by Lanthanides Ions for Bio-Medical Applications, ECS Trans., 45(2012) 191–198.

[6]. Y. Li, F. Qian, J. Xiang, M.C. Lieber, Nano wire electronic and optoelectronic devices, Mater. Today, 9 (2006) 18–27.

[7]. A. Podhorodecki, G. Zatryb, L.W. Golacki, J. Misiewicz, J. Wojcik, P. Masher, On the origin of emission and thermal quenching of SRSO:Er^{3+} films grown by ECR-PECVD, Nanoscale Res. Lett., 8 (2013) 98-1–98-12.

[8]. T. Martin, A. Koch, Recent developments in X-ray imaging with micrometer spatial resolution, J. Synch. Rad., 13(2006) 180-194.

[9]. N. Ahamed, M. Alam, K. Rajender Rao, F. Kauser, N. Ashok Kumar, N. Qazi, V. Sangal, V.D. Sharma, R. Das, V. M. Katoch, K. J. R. Murthy, S. Suneetha, S. K. Sharma, L. A. Sechi, R. H. Gilman, S. E. Hasnian, Molecular genotyping of a large, multicentric collection of Tubercle Bacilli indicates geographical partitioning of strain variation and has implications for global epidemiology of Mycobacterium tuberculosis, J. Clin. Microbiol., 42 (2004) 3240-3247.

[10]. N. McAvoy, N. Filipescu, Laser action from Terbium Trifluoroacetylacetonate in p-dioxane and acetonitrile at room temperature, Appl. Phys. Lett., 10 (1967) 160–162.

[11]. K. Kuriki, Y. Koike, Y. Okamoto, Plastic optical fiber lasers and amplifiers containing lanthanide complexes, Chem. Rev.,102 (2002) 2347-2356.

[12]. T. Welker, Recent developments on phosphors for fluorescent lamps and cathode- ray tubes, J. Lumin., 48(1991) 49–56.

[13]. L. Mancic, V. Lojpur, I. Barosso, M.E. Rabanal, O. Milosevic, Synthesis of Cerium-Activated Yttrium Aluminate Based Fine Phosphors by an Aerosol Route,Eur. J. Inor. Che, (2012) 2716-2724.

[14]. G. Gran, The use of oxalyldihydrazide in a new reaction for the spectro photometric micro determination of copper, Anal. Chim. Acta, 14 (1956) 150-152.

[15]. G. Zatryb, A. Podhorodecki,J. Serafińczuk, M. Motyka, M. Banski, J. Misiewicz, N.V. Gaponenko, Optical properties of Tb and Eu doped cubic

$YAlO_3$phosphors synthesized by sol–gel method, Optical Materials, 35 (2013) 2090–2094.

[16]. H.B. Premkumar , D.V. Sunitha , H. Nagabhushana , S.C. Sharma , B.M. Nagabhushana ,J.L. Rao, Kinshuk Gupta , R.P.S. Chakradhar , $YAlO_3:Cr^{3+}$ nanophosphor: Synthesis, photoluminescence, EPR, dosimetric studies, Spectrochim. Acta Part A, 96 (2012) 154–162.

[17]. J. Yu, X. Liang, Y. He, F. Liang, P. Jin, Precursor thermal decomposition synthesis of Eu^{3+}-doped $Y_3Al_5O_{12}$ (YAG) and $YAlO_3$ (YAP) nanophosphors and their optical properties, Mater. Res. Bull., 48 (2013)2792–2796.

[18]. A. Wang, Q. Liao, J. Feng, P. Zhang, A. Li, J. Wang,Apple pectin-mediated green synthesis of hollow double-caged peanut-like ZnO hierarchical superstructures and photocatalytic applications, Cryst. Engg. Comm., 14 (2012) 256-263.

[19]. M. Nasrollahzadeh, S. M. Sajadi, A. R. Vartooni M. Khalaj, Green synthesis of Pd/Fe_3O_4 nanoparticles using *Euphorbia condylocarpa M. bieb* root extract and their catalytic applications as magnetically recoverable and stable recyclable catalysts for the phosphine-free Sonogashira and Suzuki coupling reactions, J. Mol. Catl. A Chem., 396 (2015) 31-39.

[20]. N. Thovhogi, A. Diallo, A. Gurib-Fakim, M. Maaza, Nanoparticles green synthesis by Hibiscus Sabdariffa flower extract: Main physical properties, J. Alloys Compd., 647 (2015) 392-396.

[21]. W.C. Smith, R.W. Kinney, D.G. De Partee, Latent fingerprints - a forensic approach, J. Forensic Identif., 43 (1993) 563-570.

[22]. L.K. Seah, U.S. Dinish, W.F. Phang, Z.X. Chao, V.M. Murukeshan, Fluorescence optimization and lifetime studies of fingerprints treated with magnetic powders, Forensic Sci. Int., 152 (2005) 249-257.

[23]. T.J. Haley, N. Komesu, G. Colvin, L. Koste, H.C. Upham, Pharmacology and toxicology of europium chloride, J. Pharm. Sci. 54 (1965) 643–645.

[24]. B.D. Hietbrink, B.E. Dubois, P. Kenneth, The acute mammalian toxicity of rare earth nitrates and oxides, Toxicol. Appl. Pharmacol. 5 (1963) 750–755.

[25]. V. K. Patel, S. Bhattacharya, High-performance nanothermite composites based on aloe-vera directed CuO nanorods, ACS Appl. Mater. Interfaces, 5 (**2013)** 13364-13374.

[26]. Zhensen Liu, Junfeng Ma, Yong Sun, Zuwei Song, Jingrui Fang, Ye Liu, Chang Gao, Jingang Zhao, Low-temperature molten salt synthesis of $YAlO_3$ powders assisted by an electrochemical process, Ceram. Int., 36 (2010) 2003-2006.

[27]. H.B. Premkumar, H. Nagabhushana, S.C. Sharma, S.C. Prashantha, H.P. Nagaswarupa, B.M. Nagabhushana, R.P.S.Chakradhar, Structural, photo and thermoluminescence studies of Eu^{3+} doped orthorhombic $YAlO_3$ nanophosphors, J. Alloys Comp., 601(2014) 75-84.

[28]. R.W.G. Wyckoff, Crystal Structures, Interscience, New York, (1964) 4-5.

[29]. D. Chikte (Awade), S.K. Omanwar, S.V. Moharil, Luminescence properties of red emitting phosphor $NaSrBO_3:Eu^{3+}$ prepared with novel combustion synthesis method, J. Lumin., 142 (2013) 180–183.

[30]. L.K. Pan, Q. Sun Chang, C.M. Li, Elucidating Si−Si Dimmer Vibration from the Size-Dependent Raman Shift of Nano solid Si, J. Phys. Chem. B 108 (2004) 3404–3406.

[31]. H.Q. Cao, X.Q. Qiu, B. Luo, Y. Liang, Y.H. Zhang, R.Q. Tan, M.J. Zhao, Q.M. Zhu, Synthesis and Room-Temperature Ultraviolet Photoluminescence Properties of Zirconia Nanowires, Adv. Funct. Mater., 14 (2004) 243–246.

[32]. J. Tauc, in: F. Abeles (Ed.), Optical Properties of Solids, North-Holland, Amsterdam, 1970.

[33]. H.B. Premkumar, B.S. Ravikumar, D.V. Sunitha, H. Nagabhushana, S.C. Sharma, M.B. Savitha, S. Mohandas Bhat, B.M. Nagabhushana, R.P.S. Chakradhar, Investigation of structural and luminescence properties of Ho^{3+} doped $YAlO_3$ nanophosphors synthesized through solution combustion route, Spectrochim. Acta Part A, 115 (2013) 234–243.

[34]. H.B. Premkumar, D.V. Sunitha, H. Nagabhushana, S.C. Sharma, B.M. Nagabhushana, C. Shiva kumara, J.L. Rao, R.P.S. Chakradhar, Thermoluminescence, photoluminescence and EPR studies on Mn^{2+} activated yttrium aluminate ($YAlO_3$) perovskite, J. Lumin.,132 (2012) 2409-2415.

[35]. Dorenbos P. Systematic behavior in trivalent lanthanide charge transfer energies. J Phys. Condens Matter 15 (2003) 8417-8434.

[36]. P. Dorenbos,The 5d level positions of the trivalent lanthanides in inorganic compounds, J. Lumin., 91 (2000) 155-176.

[37]. A.A. da Silva, M.A. Cebim, M.R. Davolos, Excitation mechanisms and effects of dopant concentration in $Gd_2O_2S:Tb^{3+}$ phosphor, J. Lumin., 128 (2008) 1165-1168.

[38]. Fabio Angiuli, Enrico Cavalli, Alessandro Belletti, Synthesis and spectroscopic characterization of YPO_4 activated with Tb^{3+} and effect of Bi^{3+} co-doping on the luminescence properties, J. Solid State Chem.,192 (2012) 289–295.

[39]. D. Jia, J. Zhu, B. Wu, S. E, Luminescence and energy transfer in $CaAl_4O_7$: Tb^{3+}, Ce^{3+}, J. Lumin., 93 (2001) 107-114.

[40]. W.F. van der Weg, Th.J.A. Popma, A.T. Vink, Concentration dependence of UV and electron-excited Tb^{3+} luminescence in $Y_3Al_5O_{12}$, J. Appl. Phys., 57 (1985) 5450-5456.

[41]. Yahong Jin, Yihua Hu, Li Chen, Xiaojuan Wang, Guifang Ju, Zhongfei Mu, Luminescent properties of Tb^{3+}-doped Ca_2SnO_4 phosphor, J. Lumin., 138 (2013) 83- 88.

[42]. H. Nagabhushana, B.M. Nagabhushana, M. Madesh Kumar, C.H. Rayappa, K.V.R. Murthy, C. Shivakumara, R.P.S. Chakradhar, Synthesis, characterization and photoluminescence properties of $CaSiO_3$:Eu^{3+} red phosphor, Spectrochim. Acta Part A, 78(2011) 64-69.

[43]. H. N. Luitel, T. Watari, R. Chand, T. Torikai, M. Yada, Photoluminescence properties of a novel orange red emitting $Sr_4Al_{14}O_{25}$:Sm^{3+}phosphor and PL enhancement by Bi^{3+} co-doping, Opt. Mater., 34 (2012) 1375-1380.

[44]. D.L. Dexter, A Theory of Sensitized Luminescence in Solids, J. Chem. Phys. 21 (1953) 836–850.

[45]. G. Blasse, Philips, Energy transfer in oxidic phosphors, Res. Rep., 24 (1969) 131–144.

[46]. M. Catti, G. Gazzoni, G. Ivaldi, Structures of twinned-Sr_2SiO_4 and of-$Sr_{1.9}Ba_{0.1}SiO_4$, Acta Crystallogr., Sect. C: Cryst. Struct. Commun., 39 (1983) 29–34.

[47]. M. Chandrasekhar, H. Nagabhushana, S.C. Sharma, K.H. Sudheer kumar, N. Dhananjaya, D.V. Sunitha, C. Shivakumara, B.M. Nagabhushana, Particle size, morphology and color tunable ZnO:Eu^{3+} nanophosphors via plant latex mediated green combustion synthesis, J. Alloys Compd.,584 (2014) 417– 424.

[48]. L.G. Van Uitert, Characterization of Energy Transfer Interactions between Rare Earth Ions, J. Electrochem. Soc., 114 (1967) 1048-1053.

[49]. Y. Tian, B. Chen, B. Tian, R. Hua, J. Sun, L. Cheng, H. Zhong, X. Li, J. Zhang, Y. Zheng, T. Yu, L. Huang, Q. Meng, Concentration dependent luminescence and energy transfer of flower like $Y_2(MoO_4)_3$:Dy^{3+} phosphor, J. Alloys Compd. 509 (2011) 6096-6101.

[50]. Q. Meng, B. Chen, W. Xu, Y. Yang, X. Zhao, W. Di, S. Lu, X. Wang, J. Sun, L. Cheng, T. Yu, Y. Peng, J. Appl. Phys. 102 (2007) 093505-093506.

[51]. B. R. Judd, Optical absorption intensities of rare-earth ions, Phys Rev.,127 (1962) 750-761.

[52]. G S Ofelt, Intensities of crystal spectra of rare-earth ions, J. Chem. Phys., 37 (1962) 511-520.

[53]. Jiafeng Cao, Yuexia Ji, Jianfu Li, Zhaojie Zhu, YanWang, Zhenyu You, Chaoyang Tu, Crystal growth, Judd–Ofelt analysis and fluorescence properties of Tm^{3+}: $CaNb_2O_6$ crystal, J. Lumin., 131 (2011) 1350-1354.

[54]. Dhiraj K. Sardar, Kelly L. Nash, Raylon M. Yow, John B. Gruber, Uygun V. Valiev, Edvard P. Kokanyan, Absorption intensities and emission cross sections of Tb^{3+} ($^4f_8$) in $TbAlO_3$, J. Appl. Phys.,100(2006) 083108-5.

[55]. W. Luo, J. Liao, R. Li, X. Chen, Determination of Judd-Ofelt intensity parameters from the excitation spectra for rare-earth doped luminescent materials, Phys. Chem. Chem. Phys., 12 (2010) 3276-3282.

[56]. Yanling Lu, Yongbing Dai, Jun Wang, Yang Yang, Anping Dong, Shenghua Li, Baode Sun, Spectra and intensity parameters of Tm^{3+} ion in $YAlO_3$ crystal, Optics Communications, 273 (2007) 182-186.

[57]. A.M. Tkachuk, S. E. Ivanova, A. A. Mirzaeva, M. F. Joubert, Y. Guyot, Luminescence self-quenching in praseodymium-doped double sodium yttrium fluoride cubic crystals, Condens. Mater. Spectroscopy, 118 (2015) 393-411.

[58]. A. A. Kaminskii, Crystalline Lasers: Physical Processes and Operating Schemes,CRC Press, New York, 1996.

[59]. W. Luo, J. Liao, R. Li, X. Chen, Determination of Judd-Ofelt intensity parameters from the excitation spectra for rare-earth doped luminescent materials, Phys. Chem. Chem. Phys., 12 (2010) 3276-3282.

[60]. Wenjun Dong, Yan Cheng, Liang Luo, Xiaoyun Li, Lina Wang, Chunguang Lib, Lifeng Wang, Synthesis and self-assembly of hierarchical SiO_2–QDs@SiO_2 nanostructures and their photoluminescence applications for fingerprint detection and cell imaging, RSC Advances, 4 (2014) 45939–45945.

Table captions:

Table 1: Estimated crystallite and optical energy gap values of $YAlO_3:Tb^{3+}$ nanophosphor.

Table 2: Rietveld refined structural parameters for $YAlO_3:Tb^{3+}$(7 mol %).

Table 3: Characteristic transitions of the emission bands observed in $YAlO_3:Tb^{3+}$ nanophosphor.

Table4:Judd-Ofelt intensity parameters (Ω2, Ω4), Emission peak wavelengths (λp in nm),radiative transition probability (A_T), calculated radiative (τ_{rad}) lifetime, branching ratio (β), stimulated emission cross-sections (σ_e) and optical gain ($\sigma_e \times \tau$) of $YAlO_3$: Tb^{3+}compounds (λ_{ex} = 341 nm).

Table 5: J–O intensity parameters ($\Omega_\lambda X\ 10^{-20}\ cm^2$) for Tb^{3+} ions in different hosts.

Table.6: Method of preparation, formation temperature and morphology of the product obtained in $YAlO_3$ nanophosphors.

Figure captions:

Fig.1. PXRD patterns of (1–11 mol %) Tb^{3+} doped $YAlO_3$nanophosphor.

Fig.2. Rietveld refinement of $YAlO_3$:Tb^{3+} (7 mol %) nanophosphor.(Inset Packing diagram of $YAlO_3$:Tb^{3+} (7 mol%) nanophosphor.)

Fig.3. SEM micrographs of $YAlO_3$: Tb^{3+} (7 mol %) with various concentrations of *A.V.* gel (a) 10 ml (b) 15 ml (c)20 ml (d) 25 ml (e) 30 ml and (f) naturally occurring dry soil photograph.

Fig.4. The network of the pectin polysaccharide along with the trapped $YAlO_3$:Tb^{3+} particles which resembles the concepts of egg model.

Fig.5.TEM images (a-c) of (1, 7 and 11 mol %), (d) EDAX (7 mol %); table shows element with atomic weight % of Tb^{3+} doped $YAlO_3$nanophosphor.

Fig.6. Energy band gaps of (1–11 mol %) Tb^{3+} doped $YAlO_3$nanophosphors. Inset Uv–Vis absorption spectra of (1-11 mol %) Tb^{3+} doped $YAlO_3$.

Fig.7. FTIR spectra of $YAlO_3$: Tb^{3+} (1-11 mol %) nanophosphors.

Fig.8. PL emission spectra of $YAlO_3$:Tb^{3+} (1–11mol %) nanophosphors recorded at RT. Inset Excitation spectrum of $YAlO_3$:Tb^{3+} (3 mol %) at λ_{emi}= 543nm

Fig.9. Effect of Tb^{3+}concentration on the 341 nm emission and Variation of asymmetric ratio with Tb^{3+}concentration in $YAlO_3$nanophosphors

Fig.10. Relation between log(x) and log (I/x) in $YAlO_3$: Tb^{3+} (1–11 mol %) nanophosphors.

Fig.11. CIE diagram of $YAlO^3$: Tb^{3+} (7mol %) nanophosphors. The inset figures (a & b) are the photographs of the phosphors ($YAlO_3$:Tb^{3+} (7 mol %)) under visible light and 254 nm UV lamp radiation.

Fig.12. CCT diagram of $YAlO_3$: Tb^{3+} (7 mol %) nanophosphor.

Fig.13. Finger print images developed by $YAlO_3$: Tb^{3+}nanophosphor from glass, knife handle, freshly cut green leaf and polythene sheet

Fig.14. Fingermark deposited on glass and stained by $YAlO_3$: Tb^{3+} under different illuminations

Table 1: Estimated crystallite size and optical energy gap (E_g) values of $YAlO_3:Tb^{3+}$ nanophosphor.

$YAlO_3$: Tb^{3+}	**Crystallite size(nm) [D-S approach]**	**Energy gap (eV)**
1	28	5.45
3	27	5.48
5	27	5.50
7	26	5.53
9	25	5.55
11	24	5.59

Table 2: Rietveld refined structural parameters for $YAlO_3:Tb^{3+}$ (7 mol %).

Atoms	**Oxidation state**	**Positional Parameters**			**Occupancy**
		x	**y**	**z**	
Y	+3	-0.010	0.0524	0.2531	1.0977
Al	+3	0.5000	0.0000	0.0000	1.9904
O1	-2	0.0719	0.4793	0.2500	1.7294
O2	-2	0.7891	0.2192	-0.040	3.5255

Crystal system: Orthorhombic, Lattice parameter, a = 5.1774 (1) (Å), b = 5.3224 (4) (Å), c = 7.3665 (4) (Å), Cell volume = 202.99 (3) ($Å^3$), Space group = Pbnm, $R_{Factors}$= 5.10, R_{Bragg}= 5.03, χ^2= 1.06, R_P= 4.44, R_{WP} = 6.21, R_{Exp} = 6.02.

Table 3: Characteristic transitions of the emission bands observed in $YAlO_3:Tb^{3+}$nanophosphor.

Ion		**Transition**	**λ (nm)**
Tb^{3+}	Emission	$^5D_3 \rightarrow {}^7F_3$	463
		$^5D_4 \rightarrow {}^7F_6$	493
		$^5D_4 \rightarrow {}^7F_5$	545
		$^5D_4 \rightarrow {}^7F_4$	591

Table 4. Judd-Ofelt intensity parameters (Ω_2, Ω_4), Emission peak wavelengths (λ_p in nm), radiative transition probability (A_T), calculated radiative (τ_{rad}) lifetime, branching ratio (β), stimulated emission cross-sections (σ_e) and optical gain ($\sigma_e \times \tau$) of $YAlO_3$: Tb^{3+} compounds (λ_{ex} = 341 nm).

Tb^{3+} conc. (mol%)	J–O intensity parameters ($\times 10^{-20}$ cm^2)			rmsΔS ($\times 10^{-20}$ cm^2)	Transitions	Emission peak wavelength λ_p (nm)	A_T (s^{-1})	τ_{rad} (ms)	β	σ_e X 10^{-22} cm^2	($\sigma_e \times \tau$) X 10^{-23}
	Ω_2	Ω_4	Ω_6								
1	6.08	0.97	0.032	0.432	$^5D_4 \rightarrow {}^7F_6$ $^5D_4 \rightarrow {}^7F_5$ $^5D_4 \rightarrow {}^7F_4$	493 559 588	54.6	18.29	0.9	6.26	1.144
3	6.23	1.05	0.033	0.347	$^5D_4 \rightarrow {}^7F_6$ $^5D_4 \rightarrow {}^7F_5$ $^5D_4 \rightarrow {}^7F_4$	493 543 590	56.0	17.84	0.9	6.09	1.08
5	6.26	1.04	0.033	0.332	$^5D_4 \rightarrow {}^7F_6$ $^5D_4 \rightarrow {}^7F_5$ $^5D_4 \rightarrow {}^7F_4$	493 544 590	56.2	17.77	0.9	6.11	1.085
7	6.68	0.97	0.032	0.214	$^5D_4 \rightarrow {}^7F_6$ $^5D_4 \rightarrow {}^7F_5$ $^5D_4 \rightarrow {}^7F_4$	492 544 590	60.0	16.65	0.9	6.52	1.085
9	6.68	1.0	0.033	0.224	$^5D_4 \rightarrow {}^7F_6$ $^5D_4 \rightarrow {}^7F_5$ $^5D_4 \rightarrow {}^7F_4$	493 543 591	60.0	16.64	0.9	6.53	1.086
11	6.56	1.02	0.033	0.247	$^5D_4 \rightarrow {}^7F_6$ $^5D_4 \rightarrow {}^7F_5$ $^5D_4 \rightarrow {}^7F_4$	492 544 590	58.9	16.95	0.9	6.40	1.084

Table 5. J–O intensity parameters (Ω_λ x 10^{-20} cm^2) for Tb^{3+} ions in different hosts.

Sample	Ω_2	Ω_4	$X=\Omega_2/\Omega_4$	Trend
$YAlO_3$: Tb^{3+} [Present work]	6.41	1.008	6.35	$\Omega_2 > \Omega_4$
AlO_3 [50]	8.74	2.26	3.86	$\Omega_2 > \Omega_4$
YVO_4 [52]	1.40	4.80	0.29	$\Omega_2 < \Omega_4$
$LiYF_4$ [53]	1.65	2.15	0.76	$\Omega_2 < \Omega_4$

Table.6. Method of preparation, formation temperature and morphology of the product obtained in $YAlO_3$ nanophosphors.

Material	**Method of preparation**	**Formation temperature**	**Morphology of the product**	**Reference**
$YAlO_3:Eu^{3+}$	Solution combustion method	1000 °C	Cracks and porous network	Sang Do Han et al. [61]
$YAlO_3:Eu^{3+}$	Co-precipitation	1200 °C	Cobblestone like morphology	Fang Miao et al. [62]
$YAlO_3$	Molten salt method	400 °C	Spindle-like particles	Zhensen Liu et al. [63]
$YAlO_3$:Mn	Sol–gel method	1700 °C	Facet and compact morphology	M. Baran et al. [64]
$YAlO_3$	Pechini route	130 °C	Irregular predominantly agglomerated grains	Ramya Hariharan et al. [65]
$YAlO_3:Eu^{3+}$	Solvothermal method	1100 °C	Polygon type morphology	Haeyoung Choi [66]
$YAlO_3$	Polymeric precursor method	1000 °C	Large aggregates like morphology	J.F. Carvalho et al. [67]
$YAlO_3:Dy^{3+}$	Sol–gel combustion method.	900 °C	irregular shape	Yuexia Ji et al. [68]
Gd^{3+}–Pr^{3+} codoped $YAlO_3$	Solid state reaction method	1400 °C	-	Yuhei Shimizu et al. [69]
$YAlO_3:Tb^{3+}$	Solution combustion method	1000 °C	Superstructures	Present work

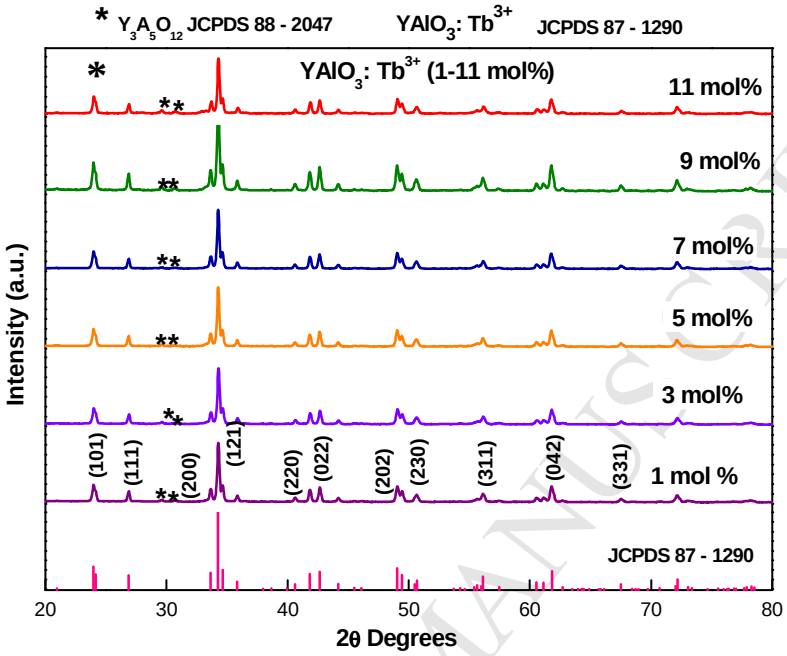

Fig.1. PXRD patterns of (1 –11 mol %) Tb^{3+} doped $YAlO_3$nanophosphor with 10 ml of *A.V.* gel.

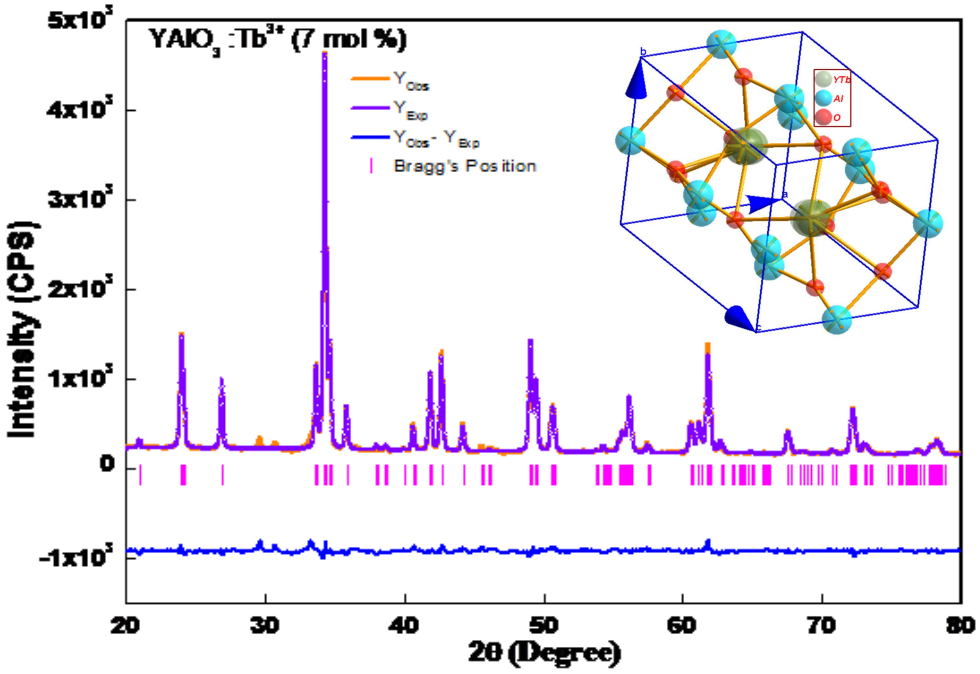

Fig. 2.Rietveld refinement of $YAlO_3:Tb^{3+}$ (7 mol %) nanophosphor. (Inset Packing diagram of $YAlO_3:Tb^{3+}$)

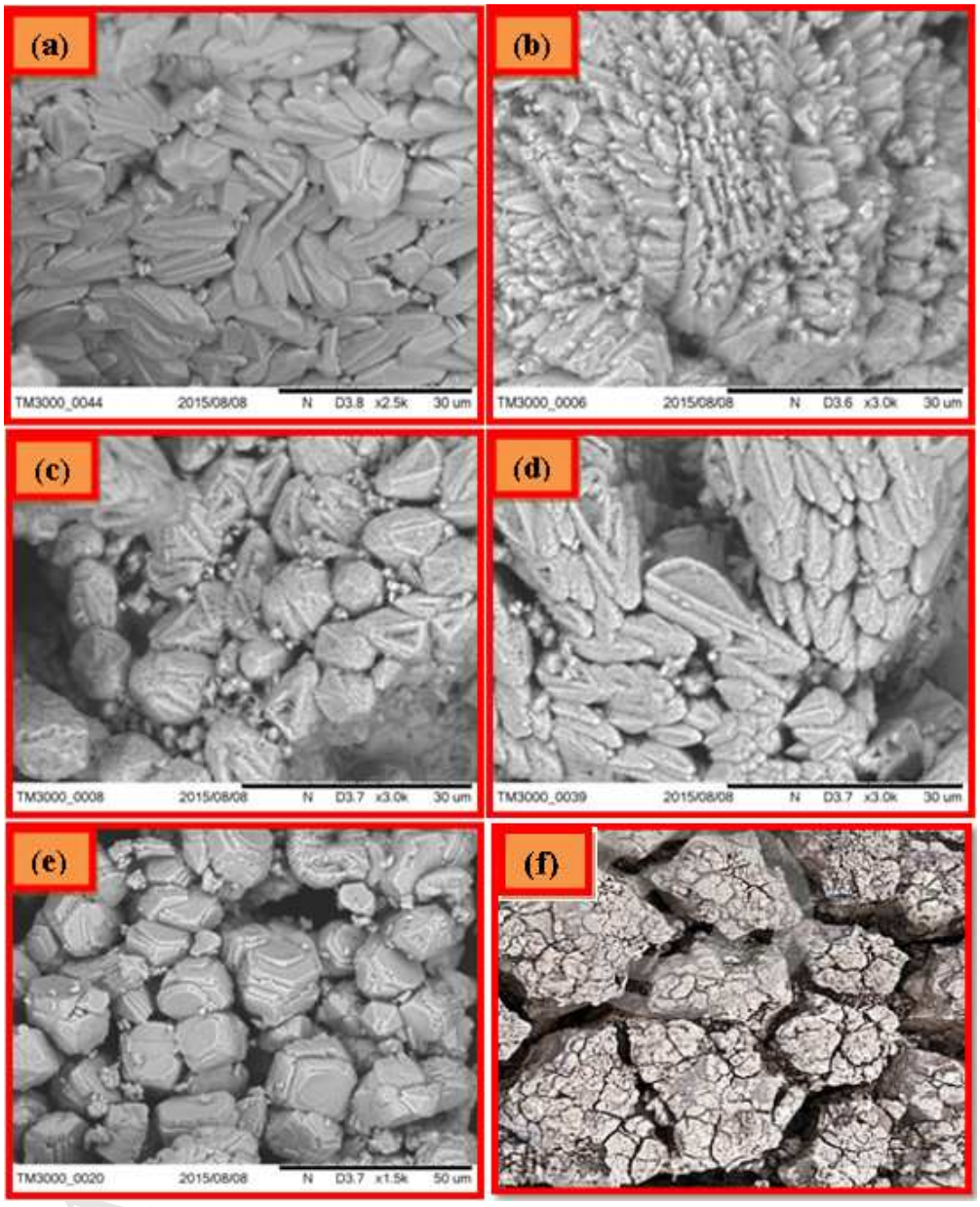

Fig.3. SEM micrographs of $YAlO_3$: Tb^{3+} (7 mol %) with various concentrations of *A.V.* gel (a) 10 ml (b) 15 ml (c)20 ml (d) 25 ml (e) 30 ml and (f) naturally occurring dry soil photograph.

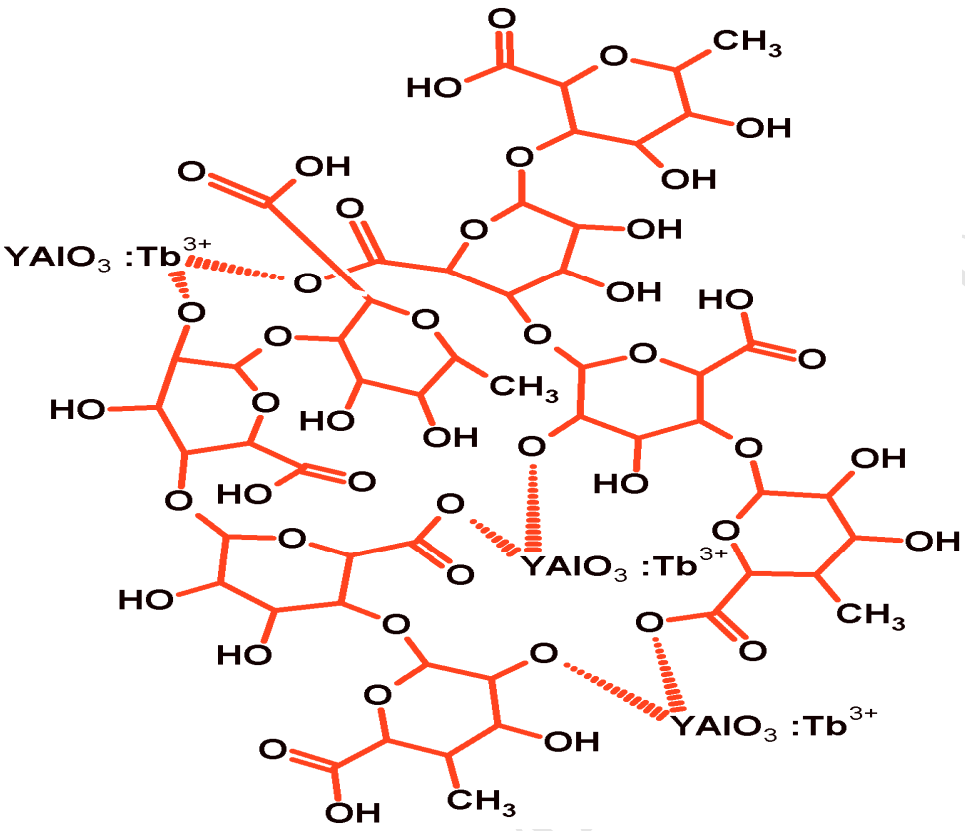

Fig.4. The network of the pectin polysaccharide along with the trapped $YAlO_3:Tb^{3+}$ particles which resembles the concepts of egg model.

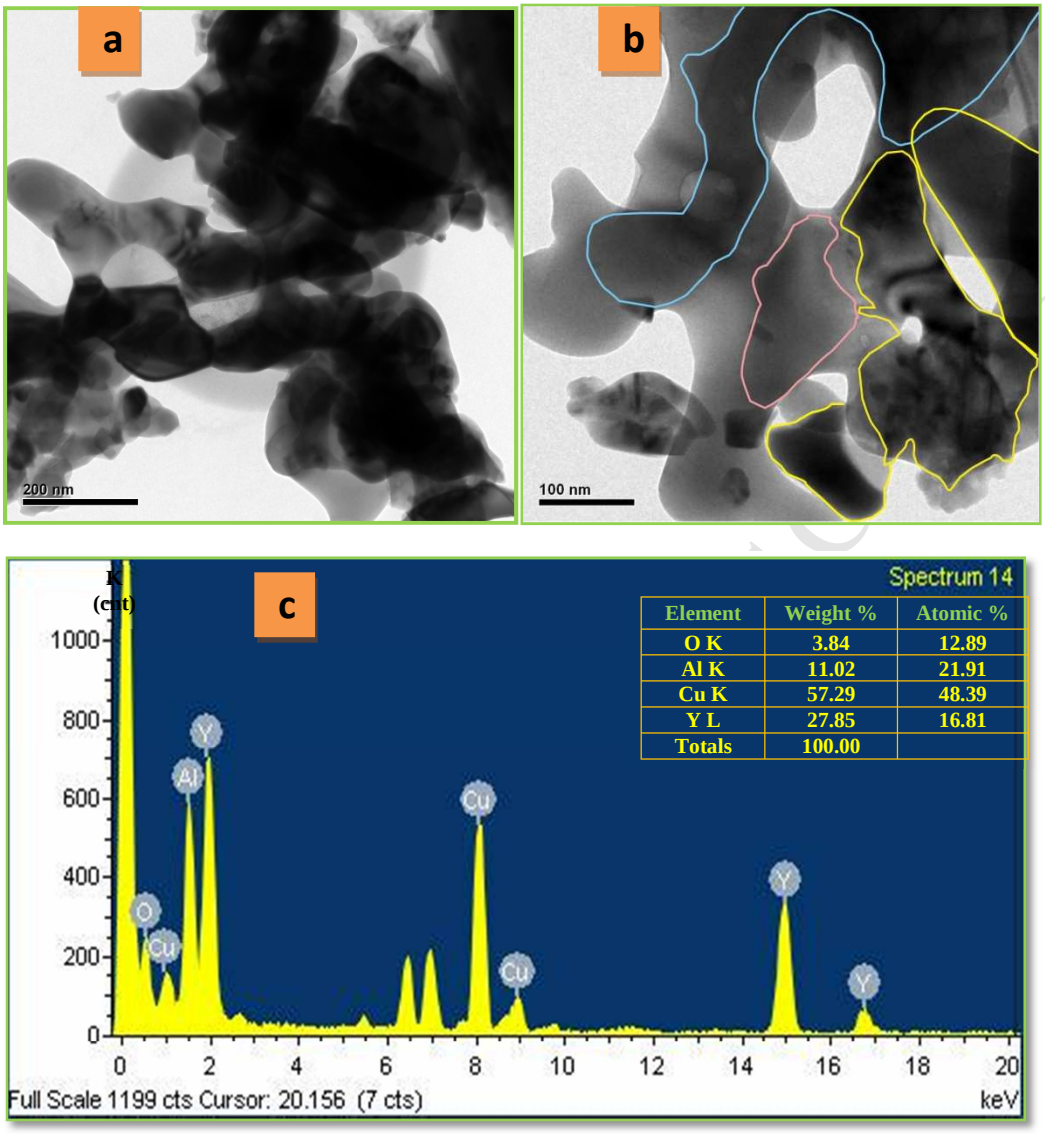

Fig.5. TEM images (a and b) of (7 mol % of Tb^{3+} ions), (c) EDAX (7 mol %); table shows elements with atomic weight % of Tb^{3+} doped $YAlO_3$nanophosphor.

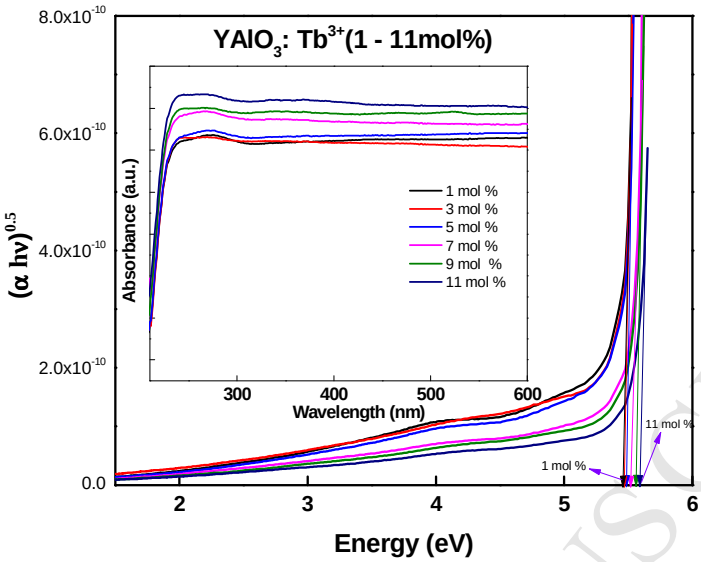

Fig.6. Energy band gaps of (1–11 mol %) Tb^{3+} doped $YAlO_3$ nanophosphors. Inset UV-Vis absorption spectra of (1-11 mol %) Tb^{3+} doped $YAlO_3$.

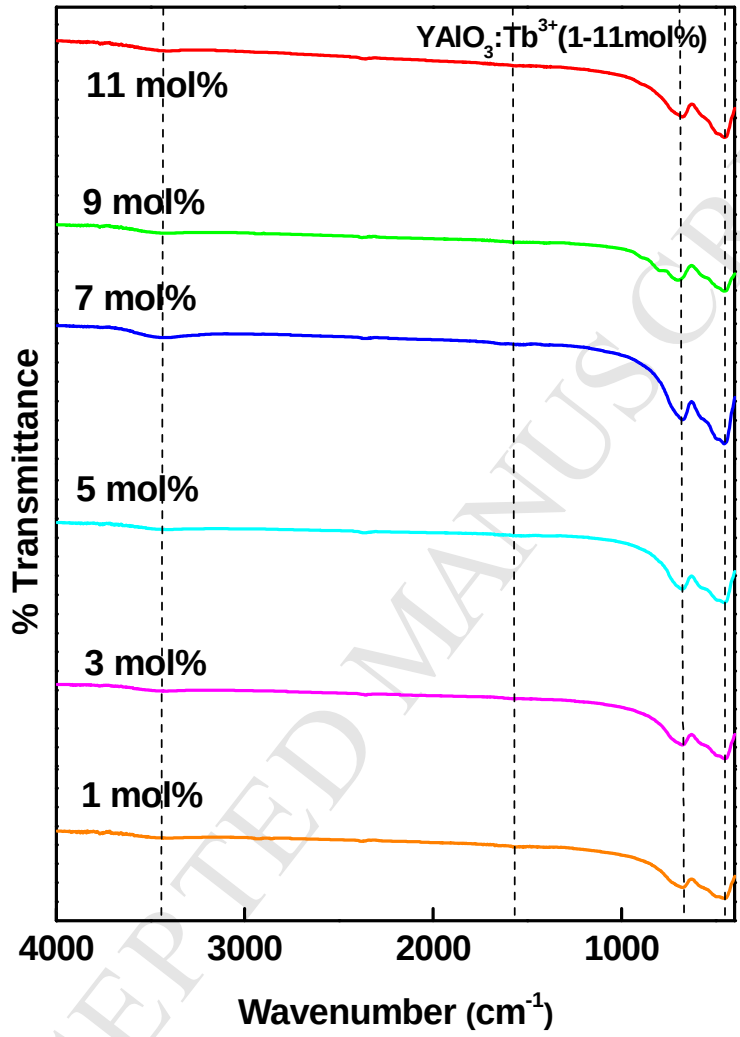

Fig.7. FTIR spectra of $YAlO_3:Tb^{3+}$ (1-11 mol %) nanophosphors.

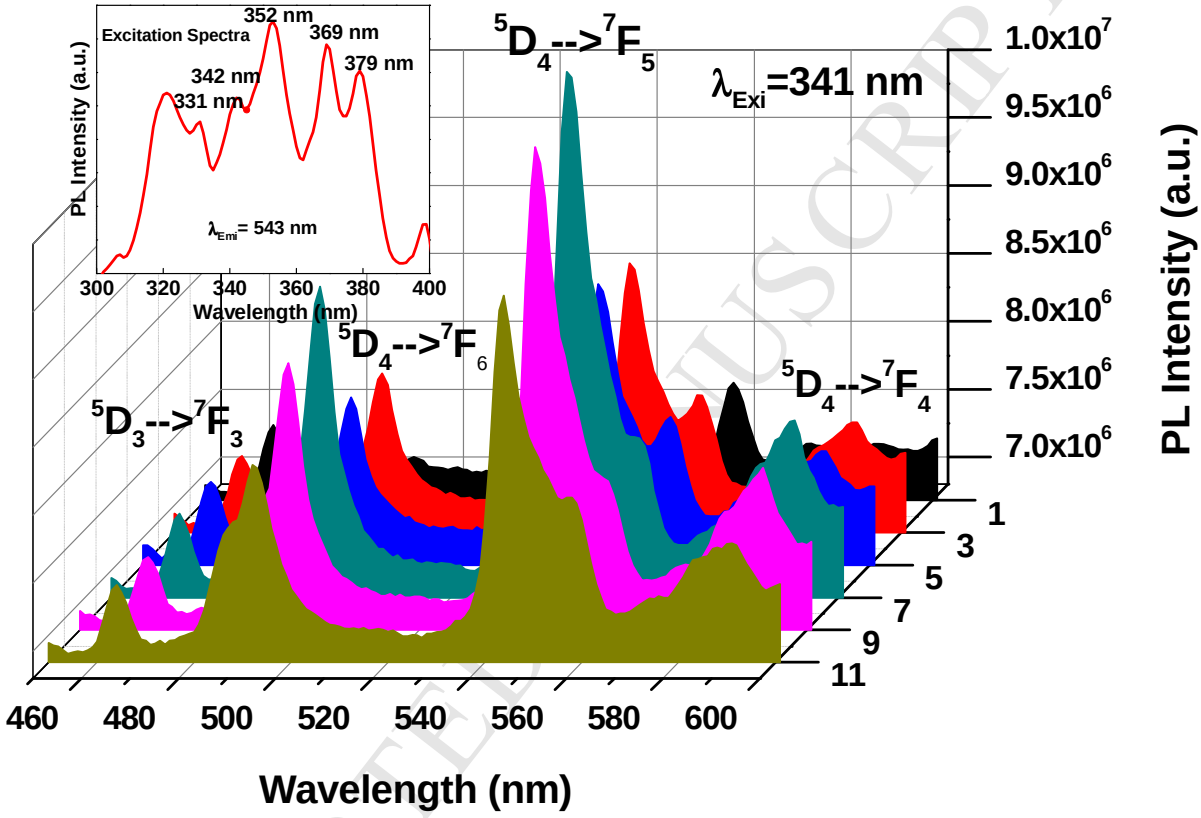

Fig.8. PL emission spectra of $YAlO_3:Tb^{3+}$ (1–11mol %) nanophosphors recorded at RT. Inset Excitation spectrum of $YAlO_3:Tb^{3+}$ (3 mol %) at λ_{emi}= 543 nm.

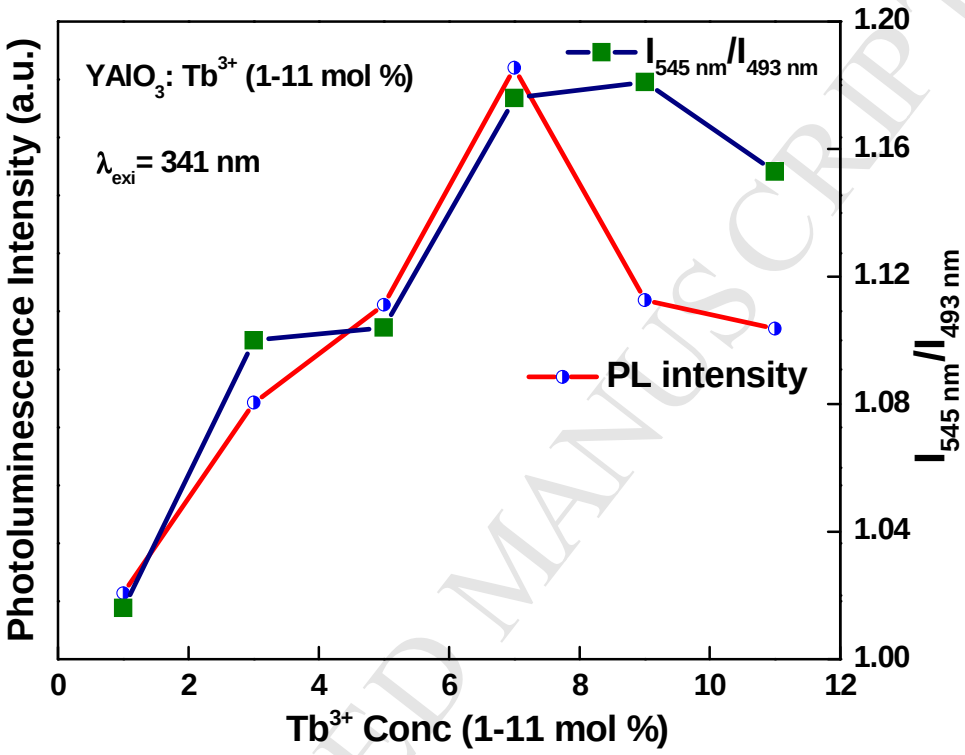

Fig.9. Effect of Tb^{3+}concentration on the 341 nm emission and variation of asymmetric ratio with Tb^{3+}concentration in $YAlO_3$nanophosphors.

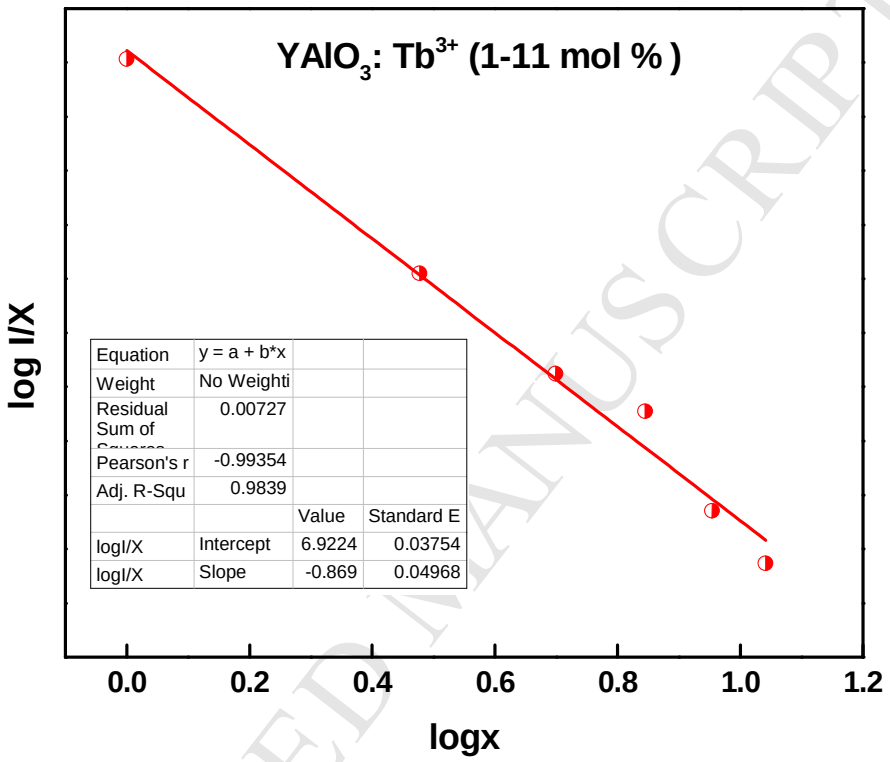

Fig.10. Relation between log(x) and log (I/x) in $YAlO_3:Tb^{3+}$ (1–11mol %) nanophosphors.

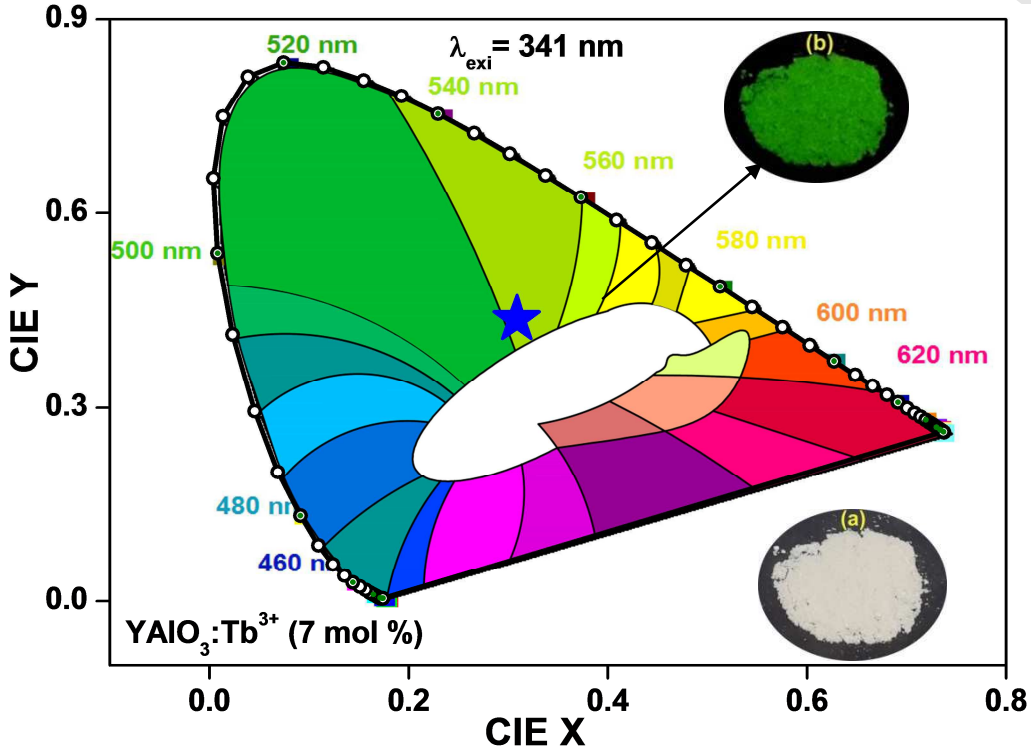

Fig.11. CIE diagram of $YAlO_3:Tb^{3+}$ (7 mol %) nanophosphor. The inset figures (a b) are the photographs of the phosphors ($YAlO_3:Tb^{3+}$ (7 mol %)) under visible light and 254 nm UV lamp radiation.

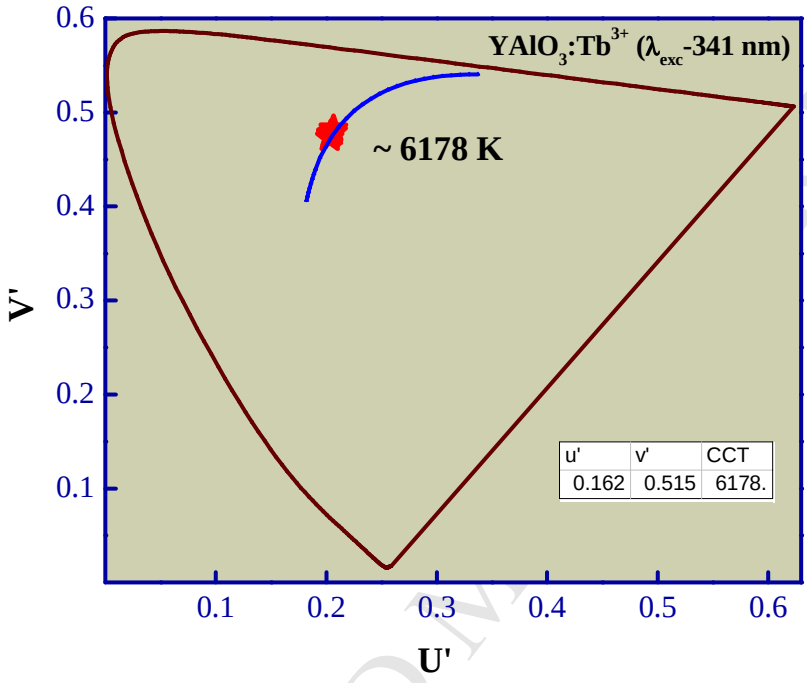

Fig.12. CCT diagram of $YAlO_3$: Tb^{3+} (7 mol %) nanophosphor

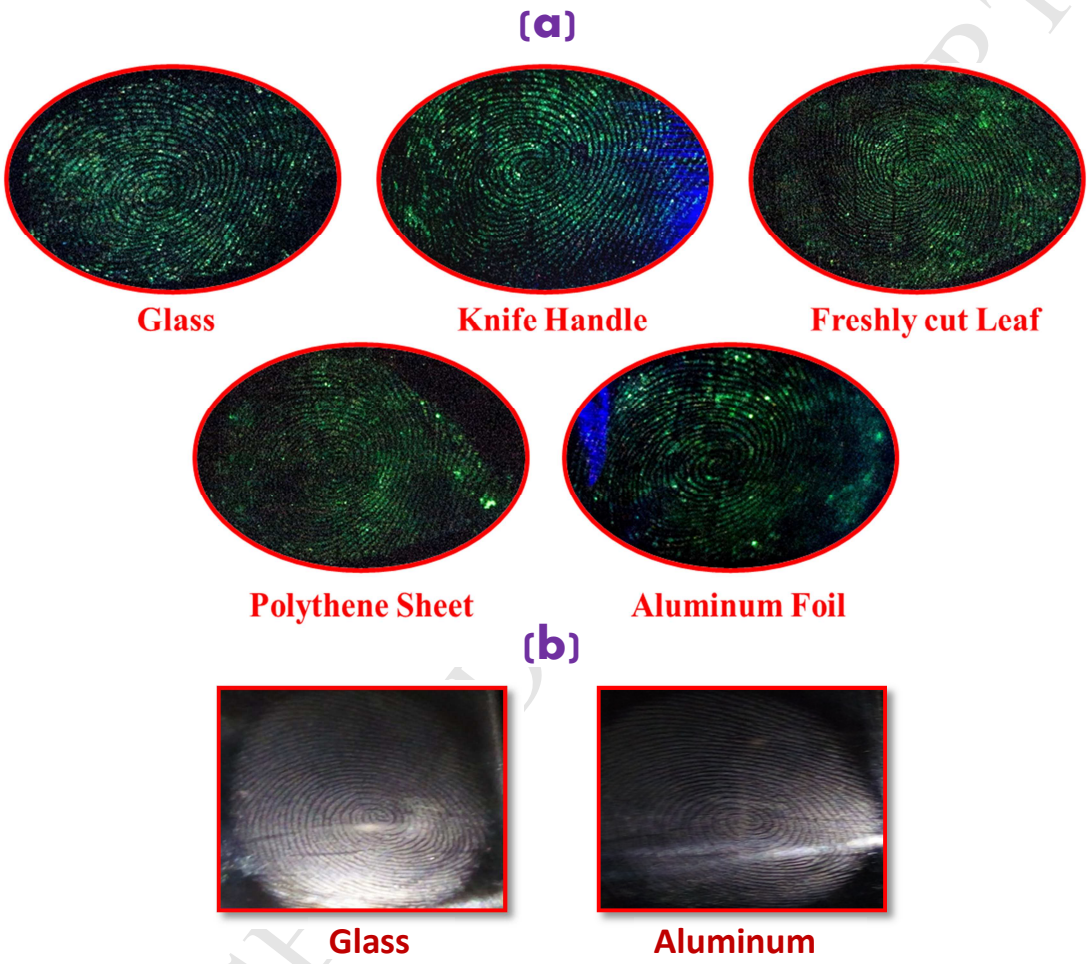

Fig.13. Finger print images developed (a) by $YAlO_3$: Tb^{3+}nanophosphor from glass, knife handle, freshly cut green leaf, polythene sheet, aluminum foil and (b) the FPs on glass and aluminum foil without the $YAlO_3$: Tb^{3+}nanophosphor.

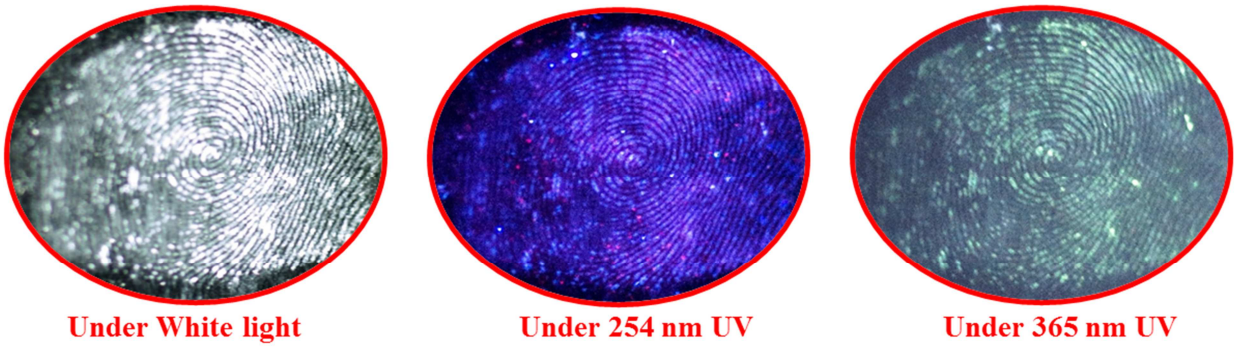

Fig.14. Fingermark deposited on glass and stained by $YAlO_3$: Tb^{3+} under different illuminations

Graphical Abstract

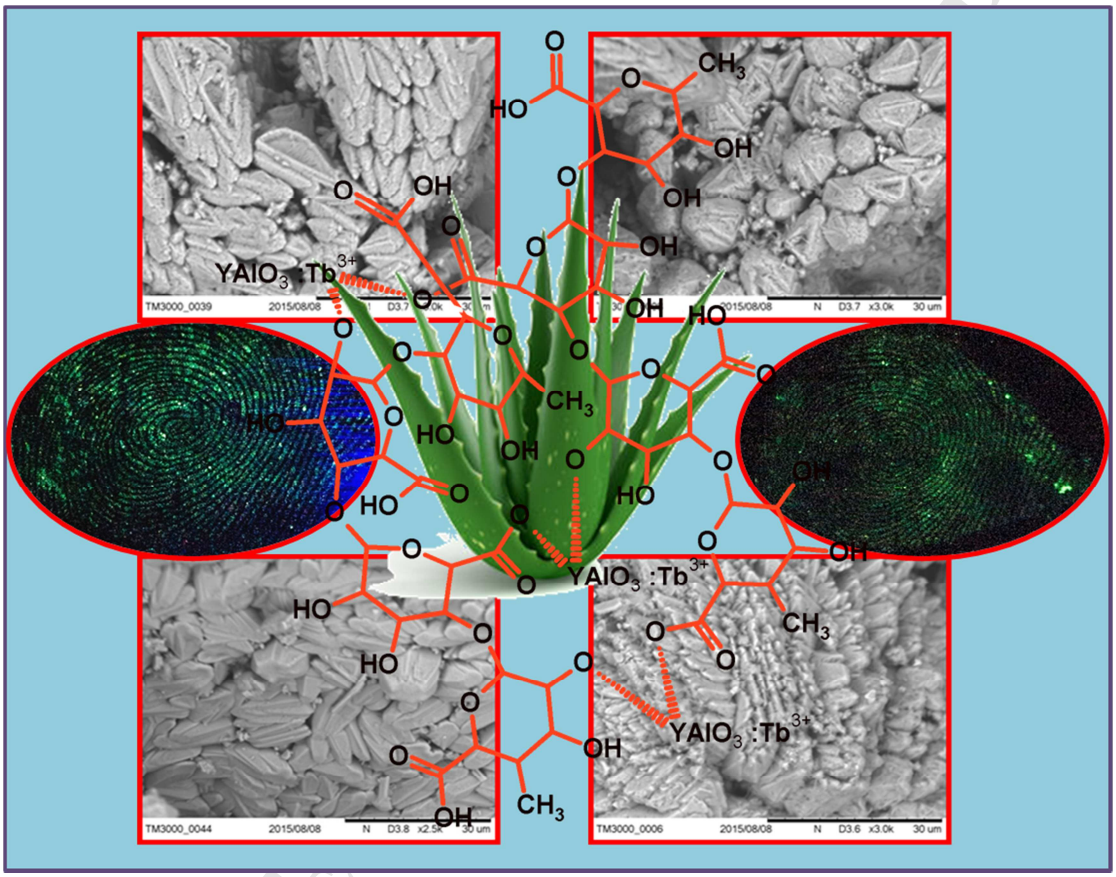

Highlights

- Doped $YAlO_3$ phosphors were obtained by green combustion route using *Aloe Vera* gel.
- Photoemission profile of $YAlO_3$: Tb^{3+} exhibit a narrow green emission peak at 545 nm.
- Detection and enhancement of fingermarks on various forensic relevant materials.
- Nanolayered superstructurs with prismatic, columnar and platy type were observed.